Advanced Composite for sp 3 -Carbon-Based Gas Sensing Application from Gold Organometallic Single Nanolayering on Diamondoids

Moad Bouzid, Didier Poinsot, Clève. Mboyi, Anna Krystianiak, Frédéric Herbst, Olivier Heintz, Bruno Domenichini, Marcel Bouvet, Jean-cyrille Hierso

Advanced Composite for sp^3-Carbon-Based Gas Sensing Application from Gold Organometallic Single Nanolayering on Diamondoids

Moad Bouzid, Didier Poinsot, Clève. D. Mboyi, Anna Krystianiak, Frédéric Herbst, Olivier Heintz, Bruno Domenichini, Marcel Bouvet,* and Jean-Cyrille Hierso**

Moad Bouzid, Didier Poinsot, Dr. Clève D. Mboyi, Pr. Dr. Marcel Bouvet, Pr. Dr. Jean-Cyrille Hierso

Institut de Chimie Moléculaire de l'Université de Bourgogne (ICMUB), UMR CNRS 6302, Université de Bourgogne, 9 avenue Alain Savary, 21078 Dijon, France

Anna Krystianiak, Frédéric Herbst, Dr. Olivier Heintz, Pr. Dr. Bruno Domenichini

Laboratoire Interdisciplinaire Carnot de Bourgogne (ICB), UMR CNRS 6303, Université de Bourgogne, 9 avenue Alain Savary, 21078 Dijon, France

Corresponding authors* E-mail:

Bruno.Domenichini@u-bourgogne.fr

Marcel.Bouvet@u-bourgogne.fr

Jean-Cyrille.Hierso@u-bourgogne.fr

Keywords: diamondoids, gold, nanocomposite, nanolayer, sensors

Abstract

The assembly of hybrid materials combining a pure sp^3-C platform from nano- and microcrystals of molecularly-defined nanometer-sized functionalized diamondoids (nanodiamonds) coated with a gold transition metal nanolayer is conducted from the gas phase, following a two-steps vapor phase dry construction process. By using first the controlled vapor phase self-assembly of primary phosphine diamantane derivatives, followed by a chemical vapor decomposition of a suited gold organometallic complex ($MeAuPMe_3$) over the self-assembled functionalized diamondoid scaffold (9-(hydroxydiamant-4-yl)phosphine, named herein H_2P–DiamOH, **1**) we achieved the synthesis of the nanocomposite Au@H_2P–DiamOH **2**. We conducted a fully dry, low-pressure approach under mild conditions below 90 °C in the presence of a partial pressure of H_2. This approach preserves the integrity of thermally sensitive organic materials. The gold deposit analyzed in details by X-ray Photoelectron Spectroscopy (XPS) revealed the clean formation of a Au–P covalent bonding, which excludes the formation of phosphine oxide, that is conversely observed when palladium or platinum organometallic complexes replaced the gold precursor. These results were confirmed at higher depth into the nanocomposite by Hard X-ray Photoelectron Spectroscopy analysis (HaXPES), notably in the binding energy area of phosphorus P1s. The thickness d of the gold layers deposited onto the surface of diamondoids was estimated to be around d = 0.8 ± 10% nm from XPS data, which allowed combining the composite Au@H_2P–DiamOH **2** with ITO interdigitated electrodes, to produce a long-life, highly stable and reproducible, n-type behavior sensor for ammonia detection. A relative response (RR) of 150% at 30 ppm and a limit of detection of 6 ppm have been measured at room temperature (20 to 25 °C) and at 45% of relative humidity (RH). Therefore, this vapor phase-controlled mild synthetic process, implemented with a gold organometallic precursor for

ultrathin nanolayer formation, allows excellent control over the formation of robust nanocomposites usable as unique sp^3-C-based sensing materials.

1. Introduction

The mild and controlled synthesis of functional nanomaterials is a key objective for creating improved devices compatible with the energy- and atom-economy contemporary challenges.[1] Accordingly, research on nanomaterials, and their applications, have been shifting from single-component to composite nanoarchitectures.[2] In this context, the controlled structuring between transition metals and carbon-based structures contributed to the design and construction of many innovative nanocomposites. This is exemplified by the activity related to metal-organic frameworks (MOFs),[3] or the numerous materials based on metal-modified graphene, fullerene and carbon nanotube (CNT), which are applied for instance in nanoelectronics and nanocatalysis processes.[4, 5, 6] The synthesis of such nanocomposites benefits from the existence of aromatic sp^2 domains and functional groups that both can participate in bonding interactions with metals. Considering the multiple fundamental and applied interests of metal/sp^2-carbon based nanocomposites, the complementary development of large scale ordered metal/sp^3-carbon based materials is attractive in the field of metal-organic nanocomposite synthesis and applications. Nevertheless, the synthesis of metal/sp^3-carbon based nanostructures remains much less developed compared with metal nanocomposites from sp^2-carbon materials.[7]

On the other hand, current metal oxide semiconductors are low-cost, robust sensors most frequently used for the toxic gas detection. These usually operate at temperatures of a few hundred degrees Celsius, which is costly and reduces sensor lifetime. Other notable limitations are cross-sensitivities with other gases, and interference from relative humidity. We envisioned that a nanocomposite combining sp^3-carbon 3D chemically and thermodynamically robust diamondoids, coated with thin metal nanolayers would yield hybrid materials with electronically modified surfaces. These materials would then be potential innovative catalysts or sensors from

a “band-structure doping”-inspired approach, which would combine sp^3-C nanodiamond organic semiconductors,[7b-d] with transition metals. Because of the thin layer and hybrid metal-organic nature the overall resistivity will be stronger providing a more sensitive material. That is what was observed in our recent works,[8,9] and confirmed herein. We recently achieved hybrid materials from molecularly-defined functionalized diamondoids with palladium, by chemical vapor deposition of a palladium organometallic complex over the self-assembly of diamondoids scaffold.[8] Interestingly, both the diamond self-assembly and the composite with palladium layers proved gas responsive as p-type sensors and promoted reversible detection of NO_2 at 50 ppb to 100 ppm concentration with fast response and recovery processes at 100 °C.[9] However, we identified that these systems encountered severe troubles of reproducibility for the detection at ppm scale of H_2 or NH_3. This lack of robustness was potentially attributed to nonreversible slow oxidation of the composites. We identified specifically that the primary phosphine had a tendency to slowly evolve into phosphine oxide along the time, despite the protective metal layer of palladium. Because of the stronger reluctance to oxidation of gold metal, we envisioned to extend the hybrid formation of sp^3-C-based sensors to gold layering and examine the materials obtained and their formation mode, with the ultimate goal to implement efficient, reproducible and robust sensors for ammonia detection.

2. Results and Discussion

2.1. Gas sensing materials doped with gold

Gas-sensing materials doped by gold have been documented in various systems, as exemplified in Table 1.[10-31] The effect of gold nanoparticles (NPs) and coatings for enhancing gas sensor performance has been especially explored in combination with metals oxide (MO) and other semiconductors (Table 1, entries 6-23), notably in term of response time (t_{res}), recovery time (t_{rec}), relative response (RR) and limit of detection (LOD); this most often at high temperatures.

However, hybrid organic-inorganic nanocomposites have also been investigated based on polymers (polypyrroles, PPy, polyanilines, PANI, *etc.*) "doped" preferably with gold NPs (Table I, entries 1-6).[10-15] In spite of the low conductivity of polymers, the presence of gold NPs generally improved the gas sensing performance, and lowest LOD of 0.1 ppb towards ammonia at RT have been obtained by using a sensitive nanocomposite organic film guar gum/polysaccharide with gold NPs (Table 1, entry 3). On the basis of this analysis, a large room for improvement exists in the development of synthetic methods for the formation of composites intimately connecting nonpolymeric organic substrates (sp^3-C-based diamondoids) and ultrathin gold nanolayers (instead of dispersed NPs), towards promoting innovative sensing properties (Table 1, entry 7). We described in the following our unique approach towards this goal.

Table 1. Gas sensor devices incorporating gold metal for ammonia detection.

N°	Gas sensing materials	T(K)	T_{res} (s)	T_{rec} (s)	RR	LOD	Ref.
1	Au/PPy	298	60	40	46%	100 ppm	10
	AuNPs@PPy	298	7	7	2.3%	1 ppm	11
3	AuNPs@GG (polysaccharide)	298	200	180	2600% (25 ppm)	0.1 ppb	12
4	Au@SiO_2-PANI (polyaniline)	298	35	133	80% (10 ppm)	10 ppb	13
5	Au@TiO_2-PANI	298	52.2	200	50%	1 ppm	14
6	Au@In_2O_3 nanosphere-PANI	298	118	144	46% (100 ppm)	500 ppb	15
7	Au@H_2P-Diam-OH **2**	298	15	7	150% (90 ppm)	6 ppm	This work
8	Au–$MoSe_2$	298	18	16	2.6%	20 ppm	16
9	AuNPs@MoS_2	298	25	15	2%	25 ppm	17
10	AuNPs@$InSe_2$ nanosheet	298	40	60	20%	0.2 ppm	18

					(10 ppm)		
11	Au/WSe_2	298	50	80	4%	5 ppm	19
12	Au – ZnO nanorods	298	165	346	20%	5 ppm	20
13	Au(+AuNPs) – ZnO nanorods	298	1800	3600	10%	2 ppm	21
14	$AgNPs/WO_{2.72}$/ AuNPs	373	120	80	20%	10 ppm	22
15	Au/ZnO/n-Si heterojunction	423	23	43	39.2%	10 ppm	23
16	$Au@WO_3$ nanorods	453	75	1000	20%	10 ppm	24
17	AuNPs@Porous Silicon (Nd-YAG)	473	15	-	43.3%	200 ppm	25
18	$Au@MoO_3$-WO_3	723	150	120	6%	5 ppm	26
19	$Au@CeVO_4$	823	7	38	15%	5 ppm	27
20	Au-$CeVO_4$@YSZ	823	301	554	20%	100 ppm	28
21	YSZ@Au@SnO_2	823	120	60	5%	20 ppm	29
22	Au/SnO_2/Yttria-stabilized zirconia	923	2	2	65% (100 ppm)	10 ppm	30
23	$Au@ZnFe_2O_4$	973	25	49	10%	5 ppm	31

2.2. Low-temperature CVD of gold onto diamondoids from an organometallic complex

Dry coating processes for generating thin layers often result in both better structuration and higher purity of the deposits.[32] Based on the volatility of adamantane and diamantane derivatives, we devised a convenient physical vapor deposition (PVD) method for accessing uniform self-assembled nano- and microstructures of functionalized diamondoids.[33] These self-assemblies were further coated with palladium from covalent bonding with donor atoms on the diamondoids.[9] The extension of this approach to gold deposition by organometallic chemical

vapor deposition (OMCVD) requires the selection of a suitable precursor. The gold(I) organometallic precursor $MeAuPMe_3$ was chosen among others ($EtAuPMe_3$, $MeAuPEt_3$) because of its excellent volatility and clean decomposition.[34] We anticipated that $MeAuPMe_3$ provides a halogen-free deposition process, in which the addition of H_2 as reductive gas may help evacuating cleanly phosphine and hydrocarbons as volatile off-gas, at mild temperature, while the resulting high purity gold(0) deposition might be efficient for toxic gas responsive application.

The deposition of the phosphine-functionalized diamondoid 9-(hydroxydiamant-4-yl)phosphine (named H_2P–DiamOH, **1**) was achieved by PVD on pre-cut silicon discs (the processing chamber is described in Figure S1). Silicon wafers [(100), 460 to 530 µm thickness] were cut into 10x10 mm, polished on the deposition side, and cleaned without removal of the native SiO_2 coverage. Under 1 to 3 torr pressure at 80 °C, the deposition of H_2P–DiamOH allows to obtain covering resistant homogeneous deposits in only 2 min (see morphology from SEM, Figure S2). The diamondoids deposit is formed of non-oriented dispersed regular platelets of a size of *ca.* 1x2x10 µm. The morphological and surface elemental features (XPS analysis) of such microcrystals self-assembly that constitutes the core support for further metal deposition has been previously detailed.[8] To achieve gold deposition by OMCVD, pure $MeAuPMe_3$ was sublimated (pressure 10 torr) and carried out into a dried and degassed quartz tubular furnace kept at 60 °C. Argon as carrier gas and 10 vol% dihydrogen as reducing gas were employed for the gold coating formation.

2.3. XPS Analysis of diamondoids self-assembly and metal composites: the case of Au@H_2P–DiamOH, 2

The surface analysis of the self-assembly of H_2P–DiamOH, **1**, on a silicon substrate wafer before any metal deposition, has been achieved according to their core levels by high resolution XPS

(Figures S3-1 to S3-3, respectively) on carbon (C1s at 283.5 eV), oxygen (O1s at 531.3 eV), and phosphorus (P2p at 131.8 eV). XPS surface analysis in the binding energy (BE) area of carbon evidenced four components: including C–C (diamond, main component) at 283.5 eV; C–OH (with consistent 1/12 area) ranging in 285.2 to 285.4 eV; C–P (also with 1/12 area) at 282.79 to 282.9 eV. The fourth component is due to classical adventitious carbon pollution around 284.8 eV. In the BE area of oxygen two components are detected, attributed as O–H at 531.4 eV (main component) and as O=P at 530.2 eV. This component clearly indicates a partial oxidation of phosphine to phosphine oxide at the deposit surface layers. Consistently, XPS in the BE area of phosphorus reveals two components for **1**: one contribution at 129.0 eV attributed to nonoxidized R–PH_2, and another at 132.0 eV related to the R–P(=O)H_2 (major component).

The fine analysis of the direct chemical interaction between the diamondoids deposit and the various metals further coated on it is essential to achieve. Indeed, both the electronic features for sensing application and the final robustness of the resulting nanocomposite mainly depends on this interaction. In the case of palladium deposited on the diamondoids, Pd@H_2P–DiamOH, the BE attributed to C1s, O1s, P2p and Pd3d (see Figures S4-1 to S4-4) were consistent with an interfacial Pd–O–PH interaction, where palladium and phosphorus interact mainly through the oxygen atom.[8] Similar results were obtained for the analogous platinum composite Pt@H_2P–DiamOH (see Figures S5-1 to S5-4), with a Pt–O–PH interaction, which illustrates again a specific interaction of the metal with a phosphine oxide present at the interface. We interpreted this structural feature as a particular affinity of platinum group metals with oxygen traces in the deposition process, and more probably afterwards by diffusion of oxygen through grain boundaries and oxidation of the phosphine-diamondoid core. This was confirmed upon aging the samples, and related to their lack of durability in sensing application along time; we thus extended our composite syntheses to gold on the basis of its recognized resistance to oxidation.[35]

*2.3.1. XPS analysis of nanocomposite Au@H_2P–DiamOH **2** in the Au4f region*

XPS analysis for the composite Au@H_2P–DiamOH **2** first provided the oxidation state of the Au at the extreme surface of the deposit (Figure 1).

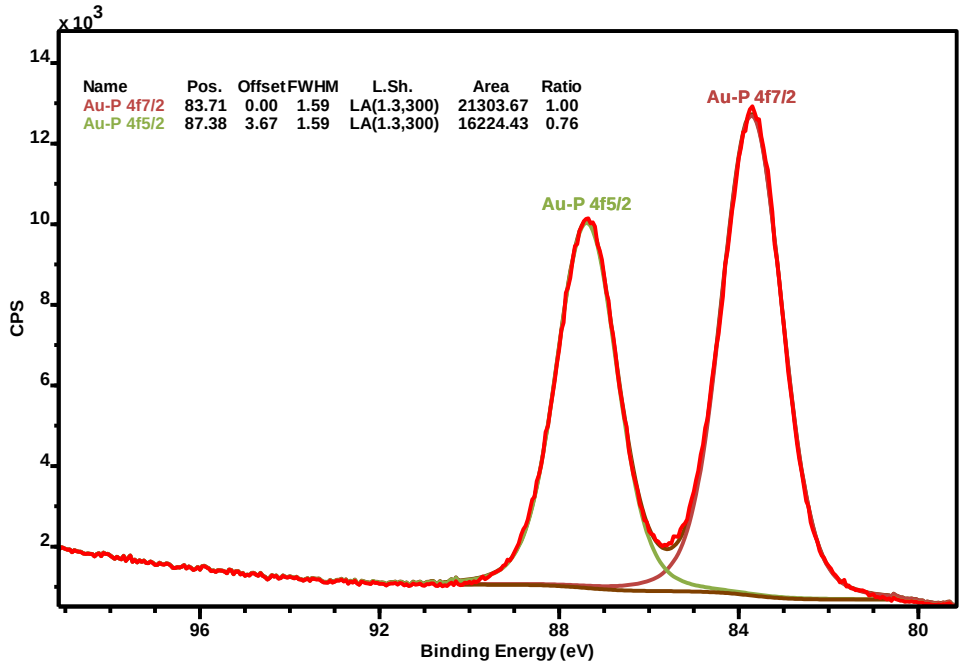

Figure 1. HR XPS spectrum of Au 4f core level for Au@H_2P–DiamOH nanocomposite **2**.

Typical X-ray photoelectron spectroscopy Au4f7/2 binding energy related to the surface of gold materials are illustrated in Table 2. These data consistently encompass a large set of gold materials of various nature: including bulk metallic gold, gold inorganic complexes, dispersed gold particles supported on inorganic substrates, and gold NPs stabilized by a variety of organic surfactants, which include thiols, thiolates, carbenes, amines, phosphines, *etc.* [36-42]

Table 2. XPS binding energies for Au materials and complexes.

entry	gold materials	Au $4f_{7/2}$ BE (eV)	Ref.
1	Bulk metallic Au(0)	84.0	36
2	Au(0) NPs	83.5-84.0	37
3	Oxidized Au(I) NPs	85.0	38
4	Thiolate-stabilized Au(I) NPs	84.6-84.9	39
5	Au@H_2P–DiamOH **2**	83.7±0.1	this work
6	Gold thin foil standard	84.0±0.1	this work
7	Au(I)Cl	84.6	40
8	$Au(III)_2O_3$	85.9	41
9	P-stabilized gold NPs@carbon	83.6	42

The values of binding energy for Au 4f7/2 corresponding to non-oxidized Au(0) are comprised between 83.5 and 84.0 eV (Table 1, entries 1-2, 7),[36,37,42] while values above 84.0 eV for Au(I),[38-40] and above 85.0 eV for Au(III),[41] are expected (entries 3-4 and 8, respectively). This is a strong indication of a charge transfer from gold "surface" to its atomic environment. These interactions indifferently involve organic and inorganic ligands for complexes and salts, and supports or surfactants for NPs.

The Au 4f7/2 binding energy for **2** was found to be 83.7±0.1 eV (Table 1, entry 5). This value is consistent with a non-oxidized Au(0) surface. This *a priori* reflected the absence of oxidized gold(I) species at the surface which contrasted with the deposition of group 10 metals (Pd, Pt) on the same diamondoid **1**, H_2P–DiamOH. We also used for zerovalent metallic Au standardization a metallic gold sample that consisted of gold thin foil (99.9%) with a 0.01mm thickness. The Au 4f 7/2 binding energies of this benchmark was found to be 84.0±0.1 eV (Table 2, entry 6) with a characteristic dissymmetric shape for the two peaks as Doniac-Sunjic profile (Figure S6).

Compared to standard Au(0), the negative shift (0.3±0.1 eV) observed for the Au 4f binding energy in Au@H_2P–DiamOH **2** is may be to a direct strong electronic interaction between gold and phosphorus. Such a charge transfer phenomenon had a few precedents in the literature. The charge-corrected Au 4f7/2 binding energy in gold(0) NPs@TiO_2 was 0.15 to 0.45 eV lower than that in bulk metallic Au(0), the decreasing of the Au 4f 7/2 binding energy and the increase in Ti^{3+} species were interpreted as direct evidences for charge transfer compensating oxygen vacancies in the support.[37c] Even more noticeable, Tang and coworkers recently reported a BE for Au 4f7/2 of 83.6 eV related to small gold–phosphorus "alloy" NPs (3 to 5 nm) supported on carbon, which a superior activity as electrocatalyst for the alkaline ethanol oxidation reaction.[42]

The direct strong interaction between gold and phosphorus Au–P, suggested by the BE relating to Au 4f 7/2 and Au 4f 5/2 at the extreme surface of nanocomposite **2**, needed to be further investigated, especially by the detailed XPS analysis of P2p and O1s regions.

*2.3.2. XPS analysis of nanocomposite Au@H_2P–DiamOH **2** in the P2p region*

We achieved the high-resolution XPS analysis of the gold supported composite Au@H_2P–DiamOH **2** in the phosphorus P2p region (Figure 2) and compared its signature with the one of its H_2P–DiamOH **1** support before gold coating.

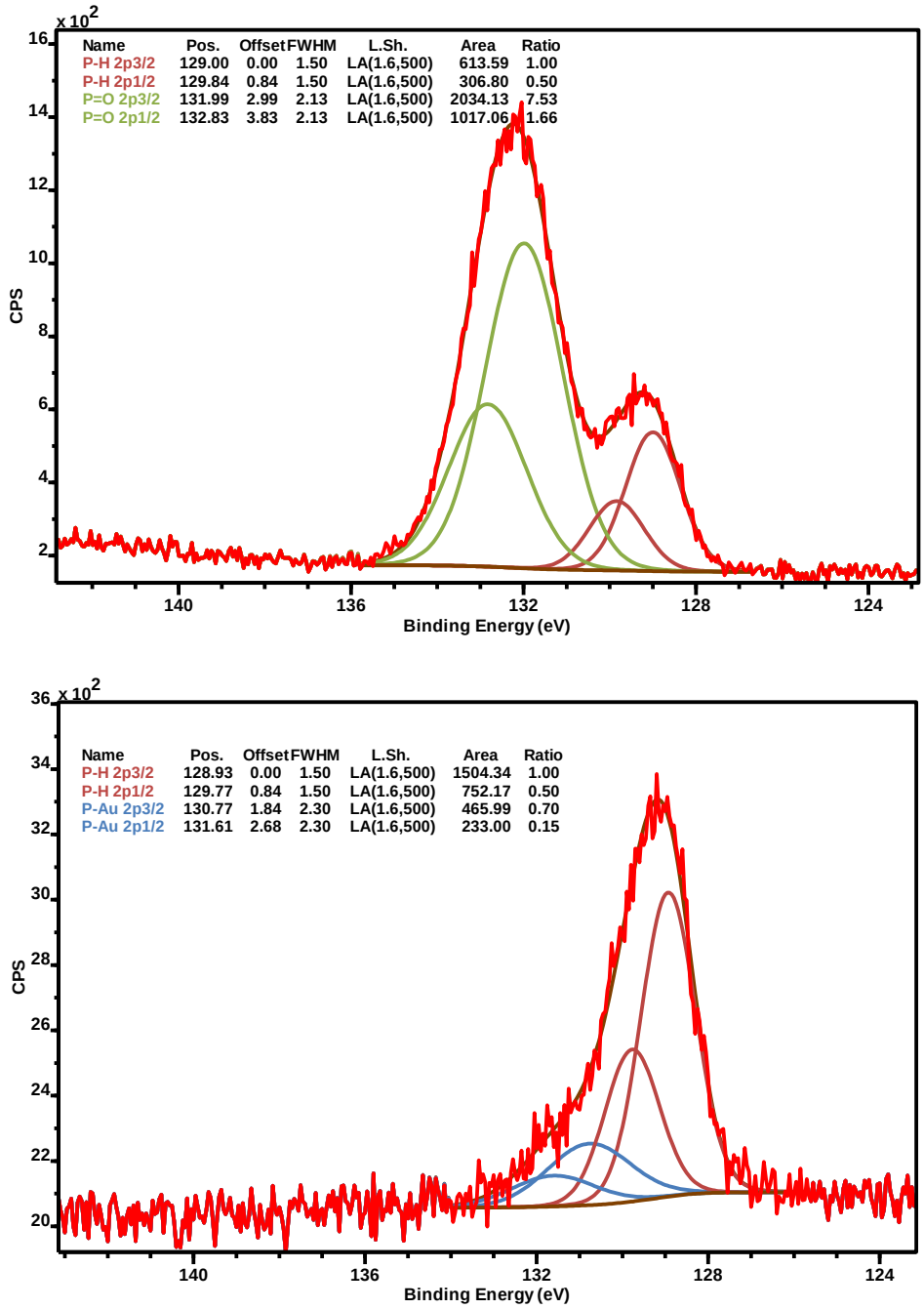

Figure 2. Comparison of the high-resolution XPS spectra at the P2p core level for the H_2P–DiamOH **1** (before gold deposition, top) and the composite Au@H_2P–DiamOH **2** (bottom).

As previously mentioned, XPS surface analysis for H_2P–DiamOH **1** in the BE area of phosphorus reveals two components, a major one at 132.2 eV related to a dominant P=O interaction [R–P(=O)H_2], and another at 129.2 eV due to non-oxidized P–H interaction (R–PH_2), for which clearly distinctive peaks are thus observed (Fig. 2, left). In the case of the composite Au@H_2P–DiamOH **2** (Fig. 2 right), not only the expected P–H interaction at 129.2 eV is detected in majority, but a higher energy contribution at 130.9 eV is also observed that could be attributed to a strong direct Au–P bonding. This, without any higher BE detectable contribution at 132.2 eV, which would then correspond to P=O interaction. This result establishes that, in addition to the resistance of gold deposition to oxidation we originally expected, a complete reduction of any phosphine oxide eventually existing in surface may occur. This hypothesis was confirmed by the XPS at the O1s region.

*2.3.3. XPS analysis of nanocomposite Au@H_2P–DiamOH **2** in the O1s region*

We achieved the comparison of the high resolution XPS surface of H_2P–DiamOH **1** and Au@H_2P–DiamOH **2** in the BE area of oxygen O1s (Figure 3, left and right, respectively)**.**

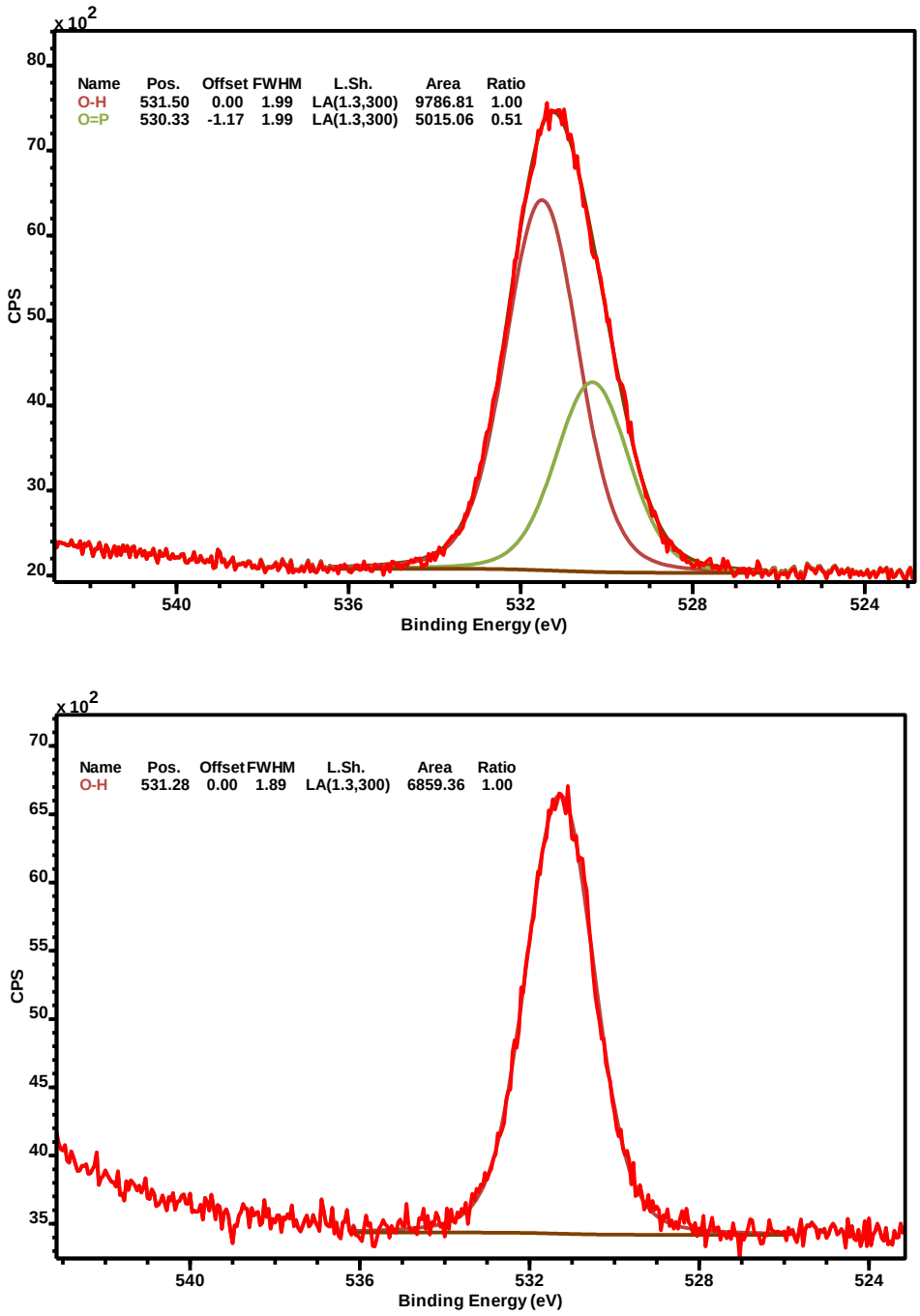

Figure 3. Comparison of the high-resolution XPS spectra at the O1s core level for H_2P–DiamOH **1** (before gold deposition, top) and Au@H_2P–DiamOH **2** (bottom).

Consistently, for H_2P–DiamOH **1,** two components are detected, related to O–H at 531.4 eV and O=P at 530.25 eV. The last component indicates an oxidation at the extreme native deposit surface of phosphine into oxide phosphine. In the case of Au@H_2P–DiamOH **2**, only a single component is detected at 531.3 eV, with a clear symmetric peak, that is related to O–H. This analysis confirmed an unexpected full reduction of phosphine oxide at the extreme surface. This also strengthens our hypothesis of an interaction between the gold layer and the diamantane phosphine deposit, which occurs without oxygen involvement, and is reasonably assumed to directly link Au and P.

*2.3.4. Hard-X-ray photoelectron spectroscopy (HaXPES) analysis of nanocomposite **2***

Full XPS analysis at gold-diamondoid composite Au@H_2P–DiamOH **2** (see also Figures S7-1 to S7-4, including C1s core level) suggested that the chemical vapor deposition process of MeAu(PMe_3) in the presence of H_2 prevents any uncontrolled phosphine oxidation. Conversely, phosphine oxidation occurs at the interface of the shell-core Pd@diamondoid composites obtained from CVD under analogous conditions. This significant difference was established at the extreme native surface, and remains valid after checking the composites kept under air for several weeks.

To further investigate the phosphine oxidation process of the composite materials the examination of phosphorus chemical environment was carried out with Au and Pd metal coatings, and compared to the native diamantanol-phosphine deposit using HaXPES apparatus (PHI Quantes). HaXPES combines two distinct radiation sources in the same apparatus: a conventional monochromatic X-ray source produced by the aluminum Kα with an energy of 1486.6 eV, and a high energy monochromatic X-ray source produced by the chromium Kα with an energy of 5414.9 eV. This approach thus combines both surface (below 10 nm) and sub-surface analysis (below 30 nm) capacities. The chromium X-ray source permits to carry out

chemical analysis through a material thickness that is about three times higher than with the aluminum X-ray source, leading to an in-depth information lacking to conventional XPS. Our measurements have been focused on phosphorus P1s core level (binding energy at *ca.* 2145 eV, Figure 4), which is the level mainly accessible using chromium X-ray source.

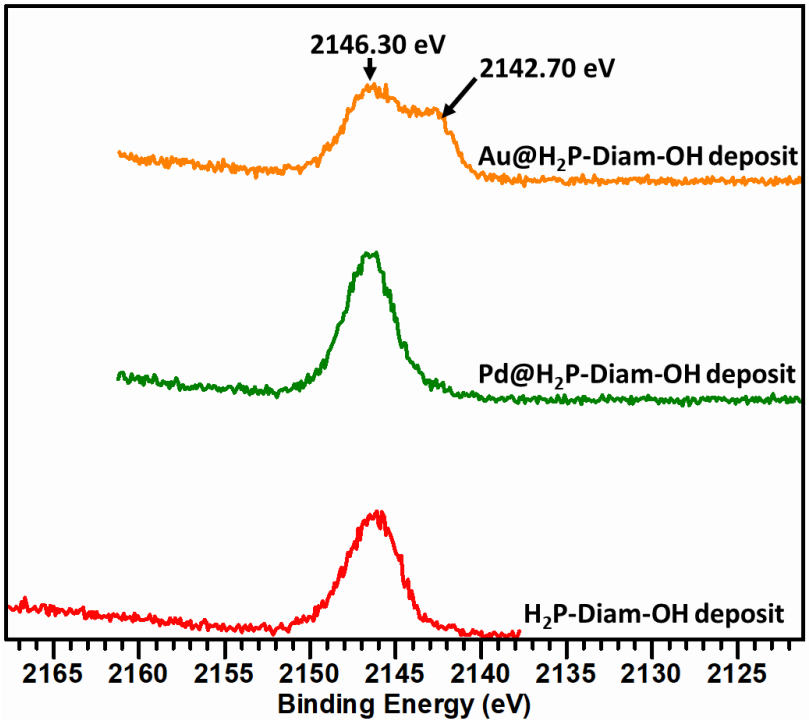

Figure 4. High-resolution HaXPES spectra at P1s binding energy area for surface of native self-assembly diamantanol-phosphine (bottom), palladium composite (middle), and gold composite (top).

The signature of Au@H_2P–DiamOH **2** at the phosphorus P1s core level revealed the presence of two components at 2142.7±0.1 eV and a major one at 2146.3±0.1 eV. Conversely, only the high energy component at 2146.3 eV is present in both Pd@H_2P–DiamOH and the native H_2P–DiamOH **1**, which is attributable to the major presence of oxidized P(V) species in the surface and sub-surface of these samples. The component at lower binding energy 2142.7 eV, is related to the nonoxidized P(III)–H interaction of the phosphine group exclusively featured in the P2p binding energy area only for the gold composite.

The fact that the sub-surfaces of the three samples present mainly oxidized phosphine signature is consistent with the hypothesis of a diffusion of oxygen through grain boundaries and oxidation of the phosphine-diamondoid core *occurring after the deposition* since this latter is achieved under Ar with a partial pressure of H_2 as reducing atmosphere. We verified our hypothesis by a long-term XPS monitoring of the native H_2P–DiamOH **1** at the P2p BE area (Figure S8). Thus, while for all the samples O_2 diffusion in the core occurs, in the presence of the gold coating the surface phosphine diamantanes are protected from further oxidation, which is not the case concerning palladium coating. This important structural difference is clearly in favor of more stable surfaces (and thus sensing behavior) for Au@H_2P–DiamOH composites **2**. The most noticeable difference in these metallo-organic core-shell phosphine-diamondoid/metal composites is probably the stability of Au–PH_2R bonding *vs* post-synthesis oxidation, compared to the higher sensitivity of platinum group metals M–PH_2R to atmospheric O_2.

2.4. SEM analysis of Au@H_2P–DiamOH 2 and coating characterization

The composite Au@H_2P–DiamOH **2** was characterized by scanning electron microscopy (SEM) for its global morphology and surface state, in comparison with its support H_2P–DiamOH **1** (Figure 5).

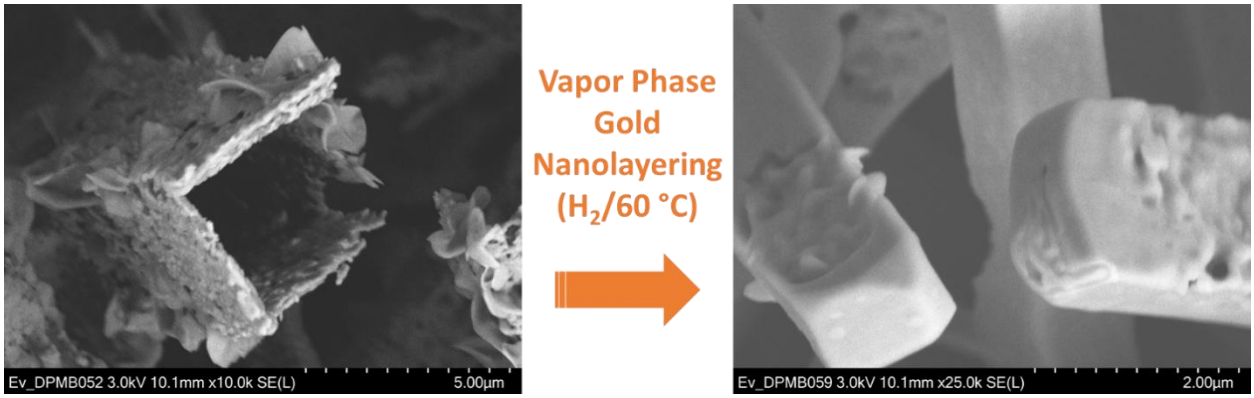

Figure 5. SEM images of deposited H_2P–DiamOH **1** (left: from PVD conditions, 85 °C, 2 min, 1-2 mbar Ar, dynamic vacuum) and composite Au@H_2P–DiamOH **2** (right: from $MeAuPMe_3$ OMCVD conditions 60 °C, 60 min, 10 torr Ar (10%vol H_2), dynamic vacuum).

The appearance of rectangular rods of the composite Au@H_2P–DiamOH **2** does not differ from the one of the phosphine diamondoid substrate H_2P–DiamOH **1** (assembly of rod-like units),[8] showing that the gold OMCVD conditions does not interfere with the first step PVD of H_2P–DiamOH **1**. However, the surface aspect is different, with a reduction of surface roughness, both on the internal and external surfaces of the rods. A seemingly homogeneous coating of gold is thus observed, with a surface smoothing of the rod. Such extended coating has been also observed for previously reported Pd@H_2P–DiamOH composite,[8] with the additional presence of nodular metallic palladium; nodules that are noticeably absent in the case of gold, which suggests much thinner and more homogeneous deposit (see below). The electronic probe micro analysis contrary to XPS is not sensitive enough for clearly detecting gold signature, suggesting again that gold may be present as a very thin layer (below 10 nm) covering the diamondoid crystals. While SEM images are not in favor of the dispersion of gold NPs but more of a homogeneous gold thin film, the question of gold deposition mode as either dispersed nanoparticles or a thin film is essential to examine in relation with further sensing applications. Indeed, an intimate Au–P interaction (absent in Au/Au-based bulky NPs) is susceptible to benefit to the composite with a type of semiconducting behavior induced.

Further treatment of XPS data is susceptible to give an estimation of a gold homogeneous coating thickness layer, and validate *a posteriori* our morphology hypothesis. Based on the principle of negative interface energy favoring a layer-by-layer growth, we hypothesized a coverage rate equal to 1, which corresponds to a total coverage of the functionalized diamondoid. The layer thickness, d, is determined from XPS by using the differential attenuation of the signals emitted by the substrate through the gold coating, especially from the photoemission signals C1s and Auger CKLL that correspond to very different kinetic energy through the deposition.[43] The extraction of d from these attenuation data can be correlated also, following the same principle, from the photoemission related to O1s and OKLL signals. We

achieved for XPS measurements various gold coatings under similar conditions, called **A**-**E** (Table 3); they cover several reproducibility issues.

Table 3: gold thickness determination carried out for different composite Au@H_2P–DiamOH **2**

	Area CKLL	Area C1s	λ_{CKLL}[a] (Å)	λ_{C1s}[a] (Å)	Thickness d (Å)
Coating **A**	50.88	579.94	5.25	14.1	**8.2**
Coating **B**	46.00	520.33	5.25	14.1	**8.1**
Coating **C**	50.94	571.49	5.25	14.1	**8.1**
Coating **D**	111.76	1106.22	5.25	14.1	**8.1**
Coating **E**	114.8	1115.8	5.25	14.1	**7.9**
	Area OKLL	Area O1s	λ_{OKLL} (Å)	λ_{O1s} (Å)	Thickness d (Å)
Coating **A**	38.5	105.2	7.75	11.91	**8.6**
Coating **B**	35.00	95.00	7.75	11.91	**8.5**
Coating **C**	42.01	118.00	7.75	11.91	**9.3**
Coating **D**	110.14	305.75	7.75	11.91	**7.7**
Coating **E**	112.32	321.7	7.75	11.91	**8.4**

[a]λ is the inelastic mean free path (IMFP) of the electrons emitted through gold coating

Coatings **A** to **D** followed the standard OMCVD conditions from $MeAuPMe_3$, *i.e.,* 10 torr pressure (Ar, 10%H_2), 60 °C, 1 h. Coating **E** was obtained from a gold deposition time extended to 3 h in order to investigate the thickness growth issue. The analysis for sample **D** was achieved with an acquisition time doubled compared to deposit **C**, *i.e.,* 20 cycles instead of 10 cycles conventionally. As shown in Table 3, the measurements and resulting values of thickness d calculated from carbon and oxygen signals are consistent between 7 and 9 Å, and among all the

samples **A** to **E**. From the results of **E** and **D**, respectively, the thickness d of the gold films deposited on the surface of the diamondoids does not depend on the deposition time or on the acquisition time during XPS measurement. The value for d = 0.8 ± 10% nm, corresponds to a single nanolayer of gold,[44] and the saturation was reached at this amount, providing an unexpected and exceptional mean of nanolayering control with a very simple CVD system. We assume that the strong intimate connection between the gold nanolayer and the primary phosphine diamondoid is at the origin of this structuring.

We were eager to investigate the properties of the composite Au@H_2P–DiamOH **2** for gas sensor application, especially concerning their response, their longevity and robustness, towards NH_3 detection, for which our first generation of composites Pd@H_2P–DiamOH were ineffective.

2.5 Gas sensing performances of composite Au@H_2P–DiamOH 2

We first determined the intrinsic resistivity of Au@H_2P–DiamOH **2** and H_2P–DiamOH **1** deposits by recording the current as a function of voltage in the range –10 to 10 V (Figure 6). For **2**, current-voltage (I-V) characteristics are slightly nonlinear, with a current of 16 nA measured at 10 V. A hysteresis was observed, which indicates a potential presence of charges able to move through the material. Additionally, the current decreases cycle after cycle and finally stabilized at *ca.* 10 nA at 10 V. Interestingly, resistivity measurements clearly show the changes achieved from Au coating, since H_2P–DiamOH **1** has a stabilized current found to be an order of magnitude smaller.

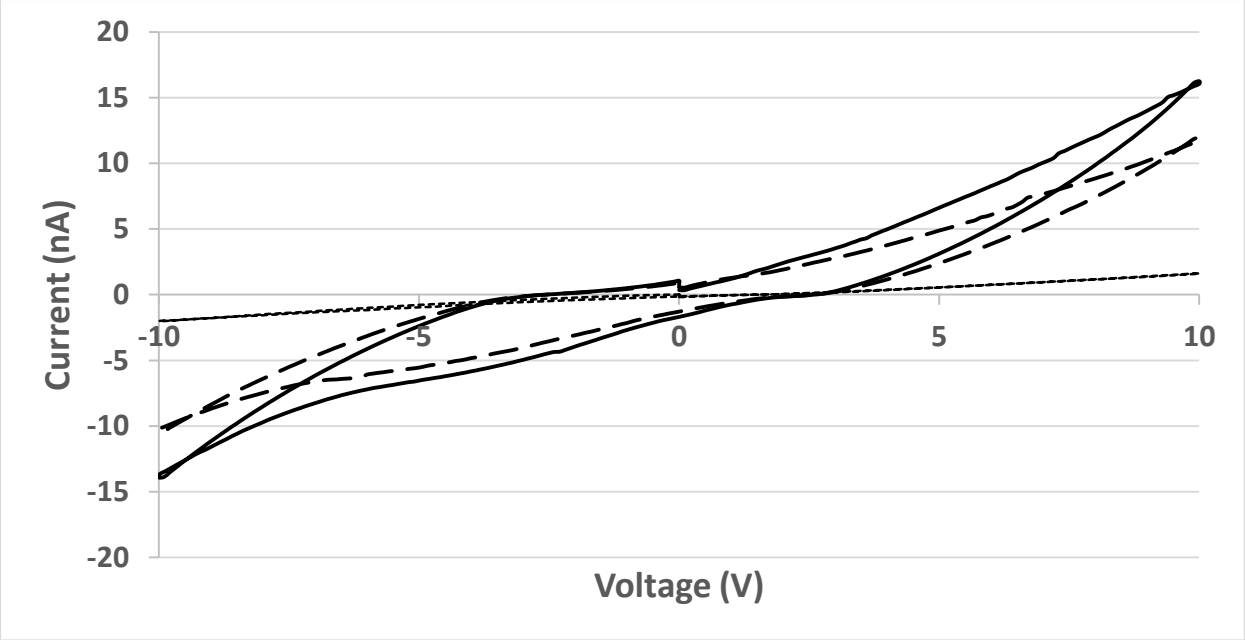

Figure 6. Current-voltage I-V characteristics of Au@H_2P–DiamOH **2**, initial curve (black line), final curve (big dash line) and pristine H_2P–DiamOH **1** (small dash line).

The low conductivity observed for deposit of H_2P–DiamOH **1** is attributed to the large thickness (*ca.* 10 µm) of resistive native diamondoid. In Au@H_2P–DiamOH **2**, the current is highly increased because of the gold nanolayer that covers the diamondoid derivative. Nevertheless, the charges need to flow across the resistive material as it is suggested in Figure 7, which depicts the device we used for testing the composite Au@H_2P–DiamOH **2** in ammonia detection (see also Figure S9 for experimental setup, and Figures S10-S12 for ITO electrode, H_2P–DiamOH@ITO and Au@H_2P-DiamOH@ITO characterization).

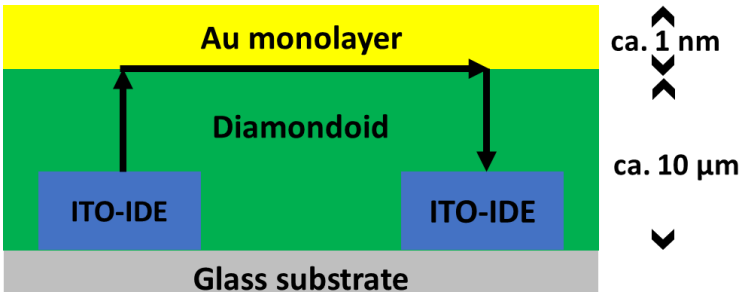

Figure 7. Schematic view of the sensing device built around composite Au@H_2P–DiamOH **2**. The black arrows represent the electron path between electrodes.[45]

Both the charges behavior and the device remind some double layer heterojunction devices that are built from the combination of a poorly-conducting molecular materials covered by a highly-conducting molecular semiconductor.[46,47] The thickness of the gold nanolayer below 1 nm in Au@H_2P–DiamOH **2** induces a significant difference from classical devices built on bulk gold (NPs or multilayered) that are in turn much highly conductive, and thus in principle intrinsically less sensitive to very small concentration (ppm) of a slightly electron-donating gas as NH_3.

*2.5.1. Au@H_2P–DiamOH **2** exposed to low concentration of ammonia NH_3*

The sensing performance of Au@H_2P–DiamOH **2** was investigated by exposing it to 90 ppm of NH_3 in three successive cycles of 10 min exposure and 30 min recovery, at RT (20 °C) in the presence of 45% humidity, and at 10 V (Figure 8).

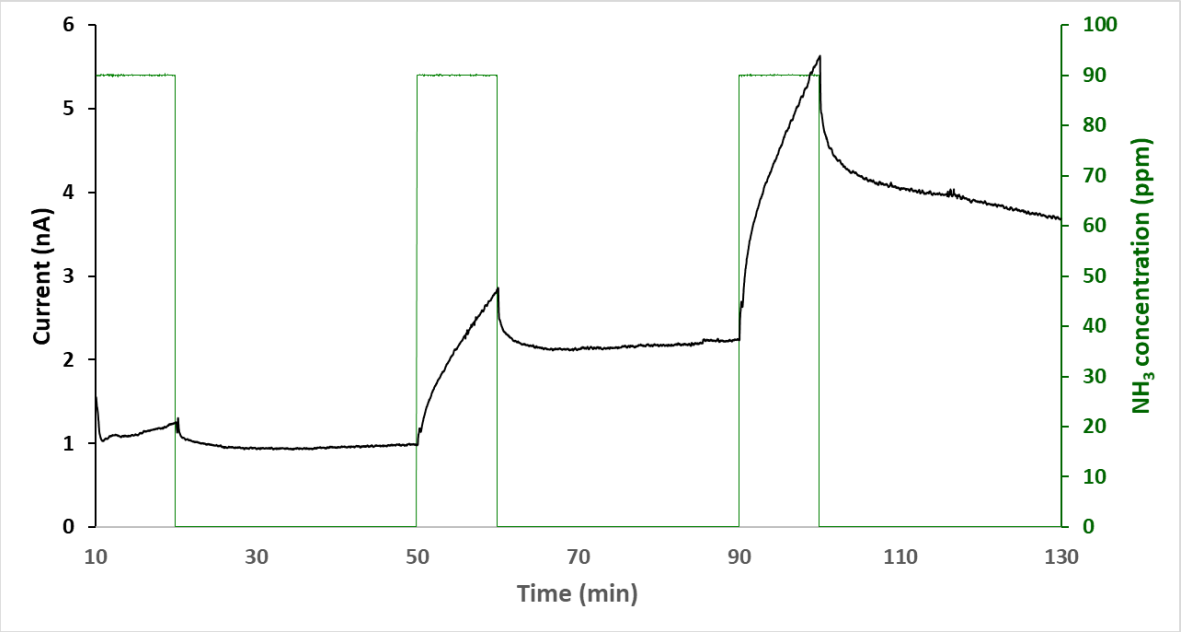

Figure 8. Current as a function of time for Au@H_2P–DiamOH **2** exposed to 90 ppm NH_3 along three successive cycles of 10 min exposure/30 min recovery at 10 V, under 45% RH at RT.

The positive response (current increase) towards NH_3 as electron-donating gas indicates the n-type behavior of the composite Au@H_2P–DiamOH **2**. A typical semiconducting p-type behavior

had been observed for Pd@H_2P–DiamOH and the pristine H_2P–DiamOH **1**,[9] establishing another notable difference between these sensing materials yet based on the same sp^3-C scaffold. The n-type behavior of Au@H_2P–DiamOH **2** was interpreted to come from a strong electron-donation of the phosphine alkyl group and the conservation of a zerovalent electron-rich gold nanolayer. This, would lead to the presence of an excess of electrons at the surface of the sensing layer and the supplementary electrons supplied by the NH_3 presence at the surface further increase the electrons density, and therefore the conductivity and current. The relative response, RR, was obtained by the following equation (1): $RR = \frac{|\mathrm{Iair} - Igas|}{Iair} \times 100\%$ (1), where I_{air} and I_{gas} are the current values of the device in air and in air containing the target gas, respectively. RR values were *ca.* +90% and +150% for the second and the third cycles, respectively, at 90 ppm; the first cycle acting thus as some conditioning period.

Gas sensing stability of Au@H_2P–DiamOH **2** was further established by successive cycles of 1 min exposure/4 min recovery, using a lower 30 ppm concentration of NH_3, at 10 V, 45% RH and RT (Figure 9).

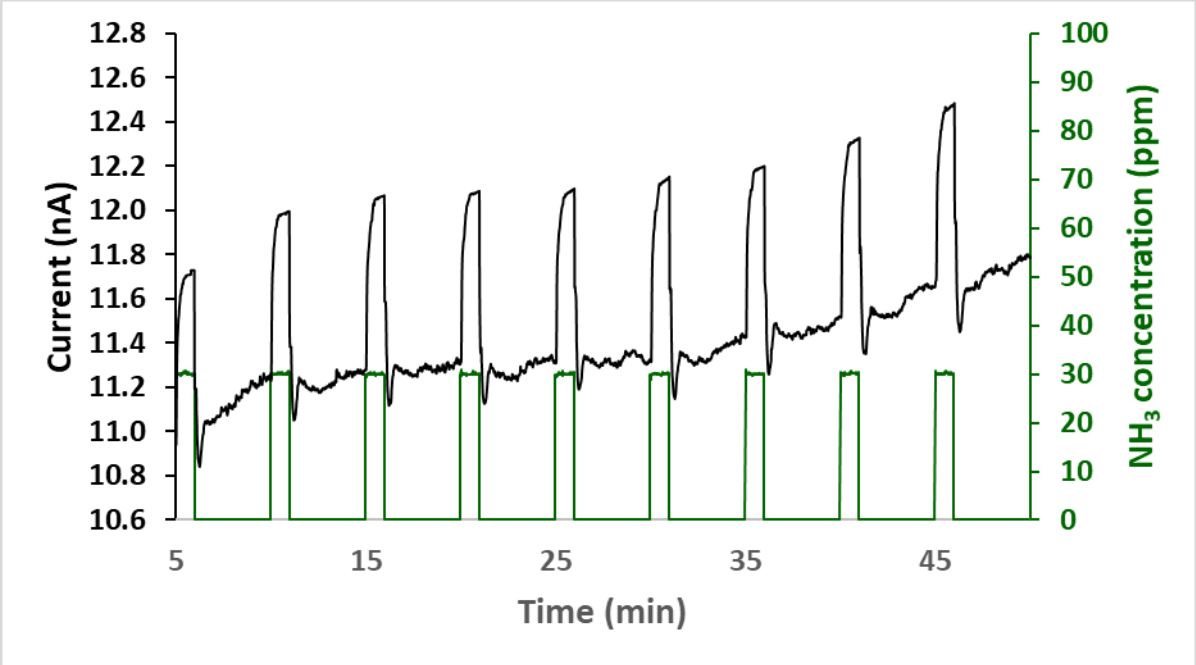

Figure 9. Current as a function of time for Au@H_2P–DiamOH **2** exposed to 30 ppm NH_3 along nine successive cycles of 1 min exposure/4 min recovery, at 10 V, under 45% RH at RT.

At the beginning of the experiment, we observed a high current variation due to the stabilization of the RH value in the test bench possibly related to humidity. Then, a stable baseline and good repeatability of the response were observed, with a RR estimated to + 9% after 1 min exposure.

Further investigations were performed with NH_3 concentrations within the range 10 to 90 ppm, every 20 ppm, keeping four cycles of 1 min exposure/4 min recovery, at 10 V, 45% RH at RT (Figure 10).

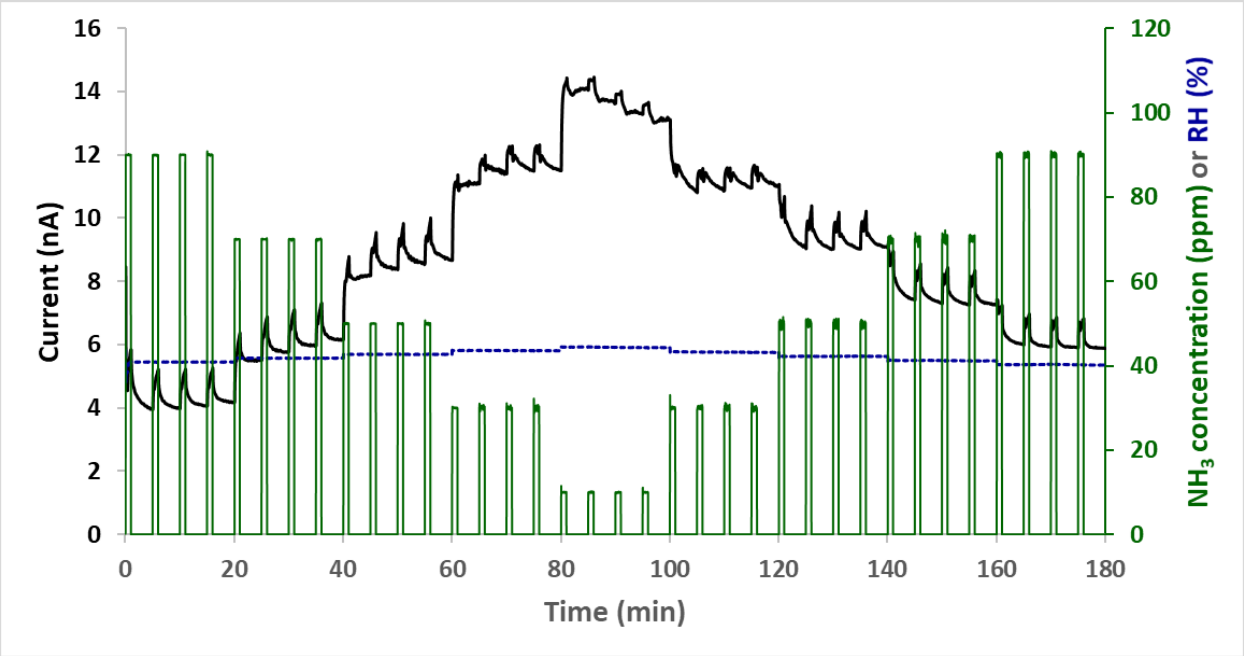

Figure 10. Current as a function of time for composite Au@H_2P–DiamOH **2** submitted to four cycles of 1 min exposure/4 min recovery within a range of 10 to 90 ppm of NH_3 at 10 V, under 40-44% RH (dotted line) at RT.

Pleasingly, all the cycles showed a stable baseline and good repeatability. The response remains clearly visible, even at 10 ppm, with a RR estimated to + 4.6%, indicating that the limit of detection (LOD) should be below 10 ppm. The weak variation of the RH value (from 40 to 44%) caused by the variation of the total gas flow when changing NH_3 concentration from 90 to 10 ppm induced a baseline shift that confirmed a significant humidity dependance of the

chemosensing behavior of the composite Au@H_2P–DiamOH **2**. Nevertheless, this humidity effect is reversible and the baseline stabilizes rapidly at each new NH_3 concentration. The current variation, $\Delta I = I_{air} - I_{gas}$, increases for the NH_3 concentration below 50 ppm, and then remains almost constant above this concentration due to a saturation effect (Figure 11).

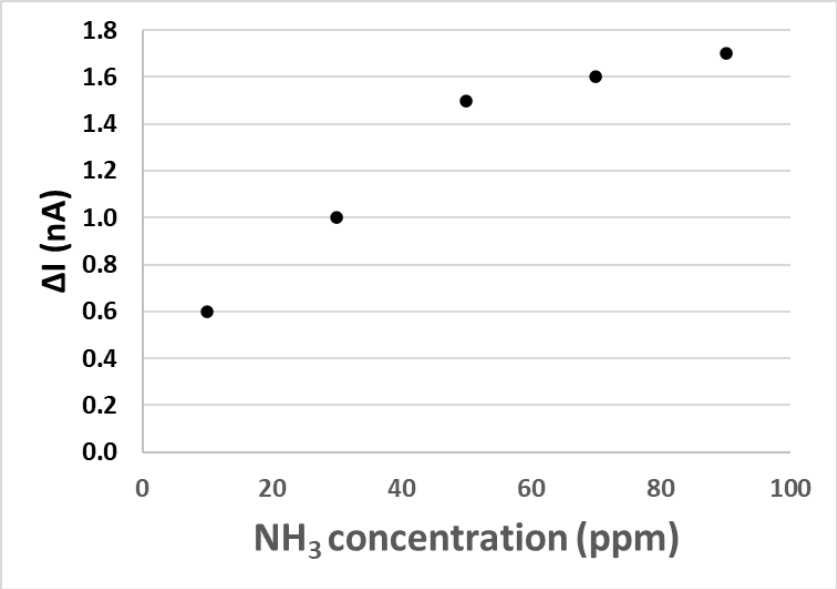

Figure 11. Current variation in devices based on Au@H_2P–DiamOH **2** as a function of NH_3 concentration, and saturation effect.

Below 50 ppm, the slope of the curve $\Delta I = f(\Delta[NH_3])$ allows to calculate the limit of detection value (equation 2), taking into account the noise, N = 4.3 10^{-2} nA, as determined from the I = f(t) curve.

$$LOD = \frac{3\,N}{S} \qquad (2)$$

where S is the sensitivity of the device ($S = \Delta I / \Delta[NH_3]$). Accordingly, a LOD of 6 ppm was calculated, which is below the threshold limit value (25 ppm) set by the Occupational Safety and Health Administration (OSHA, with exposure time equal to 8 h or 35 ppm for short-term exposure limit, lethality being above 500 ppm).

*2.5.2. Durability over the time of sensing performances of Au@H_2P-DiamOH **2***

Because the stability of the composites for sensing was a critical point at the origin of our gold coating approach, we investigated the stability in time of gold nanocomposites and therefore their durability concerning sensing performance. For palladium organohydrid, as an unstable response was observed in the first use (see Figure S13) its durability was not addressed. Concerning pristine H_2P-DiamOH **1** that has also sensing properties, after a first positive test (Figure S14, top) and 72 h storing under air the sensing performances were reinvestigated and, as expected faded away (Figure S14, bottom).

Accordingly, the sensing performances of Au@H_2P-DiamOH **2** have been investigated after one month (720 h) storing under air and are presented in Figures 12 and 13. Through successive cycles of 1 min exposure/4 min recovery, using 30 ppm of NH_3, at 10 V, 45% RH and RT a good repeatability of the detection with a small variation of baseline of the response were observed, that seems to stabilize from the 9th cycle with a RR estimated to + 8.5% after 1 min short exposure (Figure 12). A noticeable increase in the current that would need further investigation (influence of the oxygen diffusion into the diamondoid core) is observed.

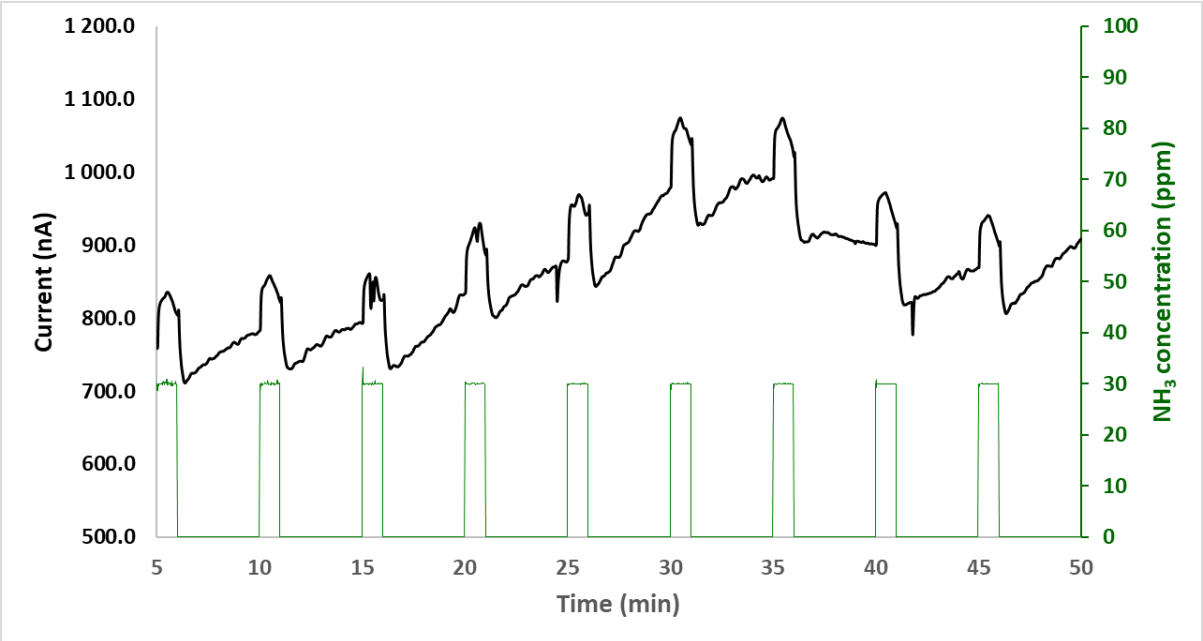

Figure 12. Current as a function of time for Au@H_2P–DiamOH **2** after one month conserved under air, and submitted to ten shorts 30 ppm NH_3 exposure/recovery cycles at 10 V and 45% RH.

We also achieved sensing experiment with different NH_3 concentrations within the range 10 to 90 ppm, every 20 ppm, keeping four cycles of 1 min exposure/4 min recovery, at 10 V, 45% RH at RT (Figure 13). All the cycles showed a stable baseline and good repeatability. The response remains clearly visible, even at 10 ppm, with a RR estimated to + 5.0%, indicating that the limit of detection (LOD) should stay below 10 ppm. A significant humidity dependence is still observed after one month for Au@H_2P–DiamOH **2** with an important baseline shift. However, we still notice that the humidity effect is reversible and that the baseline stabilizes rapidly at each new NH_3 concentration. The current variation, $\Delta I = I_{air} - I_{gas}$, increases with the concentration below 50 ppm and remains almost constant above this concentration. The slope of the curve $\Delta I = f(\Delta[NH_3])$ allows to estimate the LOD value around 4 ppm, which remains stable even after one month aging.

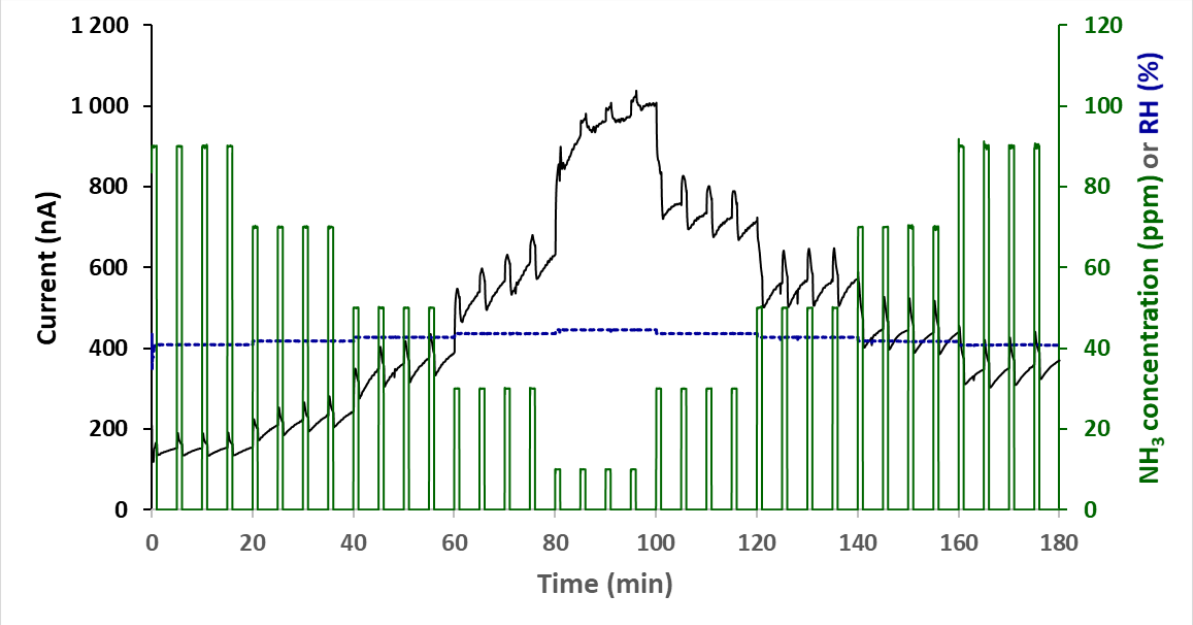

Figure 13. Current as a function of time for Au@H_2P–DiamOH **2** after one month conserved under air submitted to four short exposure/recovery cycles within a range of 10-90 ppm of NH_3 at 10 V and 40-44% RH (dotted line).

3. Conclusions

With the blossom of nanotechnology, a pathway in the development of sensor materials is achievable, towards more sensitive recognition layers from elaborate architectures, with reduced dimensionality, as low-power devices. Thus, sensitive and stable sensors, usable at moderate temperatures, for the detection of toxic gases in very low concentration are desirable.

We achieved herein, in a fully dry synthetic process, a bottom-up construction from the vapor-phase of a sp^3-carbon-based gold-diamondoid shell-core composite. This, from the self-assembly of a phosphino-diamantane (core), on which mild and clean gold single nanolayering (shell) was controlled by a simple OMCVD process using a suitable gold metalloorganic complex [MeAu(I)PMe_3] under a reducing Ar/H_2 atmosphere. The resulting composite was fully characterized by detailed XPS and Hard X-ray Photo Electron Spectroscopy HaXPES, demonstrating the controlled growth of a single 0.8 nm nanolayer of gold(0), strongly attached by a highly electron-donating –PH_2R tether. The gold-phosphine combination was shown to be highly resistant to oxidation from atmospheric oxygen along time: while the diffusion of oxygen into the phosphine-core has been evidenced by HaXPES analysis, the gold-phosphorus surface remains mostly unchanged. Accordingly, the composite Au@H_2P-DiamOH **2** integrated with ITO interdigitated electrodes, produced a sensitive n-type behavior sensor for ammonia detection with a relative response (RR) of 150% at 30 ppm and a limit of detection of *ca.* 5±1 ppm at room temperature (20 to 25 °C) and 45% of relative humidity (RH). The long-life (over one month at the atmosphere), highly stable and reproducible sensing performances are a decisive advance compared to the first generation of platinum metal-based sp^3-C-diamondoid low-power sensing devices.

4. Experimental Section

4.1. Materials characterization

XPS and HaXPES spectra were recorded with a PHI QUANTES using either Al Kα X-ray (1486.6 eV) or Cr Kα X-ray (5414.9 eV). The average circular spot size is 200 μm diameter and 45° emission angle. Survey spectra were acquired using a Pass energy of 280.0 eV with an electron step equal to 1.00 eV/step. Core levels scans using monochromatic Al Kα X-ray were acquired using a pass energy of 55.0 eV with an electron step equal to 0.05 eV/step. Core levels scans using monochromatic Cr Kα X-ray were acquired using a pass energy of 112.0 eV an electron step equal to 0.10 eV/step. These measurements were carried out at room temperature inside a vacuum vessel under pressure of 10−6 Pa. As the samples are insulators, a low-energy (<10 eV) electron flood was used to neutralize the surface charge caused by photoionization. The XPS data were then calibrated according to the sp^3 component of C1s line (283.5 eV). A standard CASA-XPS software package was used for data analysis, especially the decomposition of lines in several components as well as calculations of atomic ratios using R.S.F. (relative sensitivity factor) given by the software. SEM images were recorded with a JEOL JSM 7600F. Electron probe micro analysis "EPMA" spectra were recorded using SDD Oxford (80 mm^2, 129 eV KαMn).

4.2. Composite elaboration from the vapor phase

Metal complexes from commercial sources were used, and diamondoid synthesis are achieved following literature procedures.[8,9] The self-assembly of diamondoids and formation of composite by OMCVD are detailed in the Supporting Information.

4.3 Gas sensing experiments

Substrates composed of 1x1 cm^2 glass covered by lithography process of Indium Tin Oxide (ITO) interdigitated electrodes (IDE) with a distance of 75 μm between the electrodes were used.

Au@H_2P–DiamOH assembly have been achieved on ITO-IDE@glass substrate (see also Figure S10-S12). Thus, samples were introduced in a test chamber connected to an experimental setup dedicated to electrical and gas sensing measurements as previously detailed[48] (see Figure S11). The test bench is composed of various mass flow controllers, electronic valves and a test chamber with a size of 8 cm^3. Ammonia source (commercial source, concentration 985 ppm in synthetic air) and a synthetic air (commercial source) for dilution were injected to the test chamber. A customized homemade software precisely controls the desired ammonia concentration in the range of 1-90 ppm injected in the test chamber by regulating the flow of 500-550 mL/min through multiple fluidic lines. The relative humidity in the test chamber was monitored by an external humidity generator water tank, calibrated by a commercial humidity sensor (HMT-100, Vaisala, Finland) connected to a supplementary fluidic line in the test bench. All sensing experiments were performed at room temperature (RT, 20 to 25 °C) and at 45% of relative humidity (RH, with an external variable relative humidity in room test of 30-70%). The electrical and sensing measurements were performed using a Keithley 6517b electrometer with an incorporated DC voltage supply. Gas sensing measurements were accomplished in a dynamic way with alternating exposure steps of 1 or 10 min and recovery steps of 4 or 30 min, respectively.

Acknowledgements

This work was supported by the CNRS (ICMUB and ICB), the Université de Bourgogne, the ANR PRC program 2020 CARAPH (ANR-20-CE07- 0001-01), the Conseil Régional Bourgogne–Franche-Comté, and the PIA-excellence ISITE-BFC (COMICS project “Chemistry of Molecular Interactions Catalysis and Sensors”, and The Fonds Européen de Développement Régional (FEDER). Thanks is due to ARCEN and PACSMUB platforms for the analytical work.

Table of contents graphic

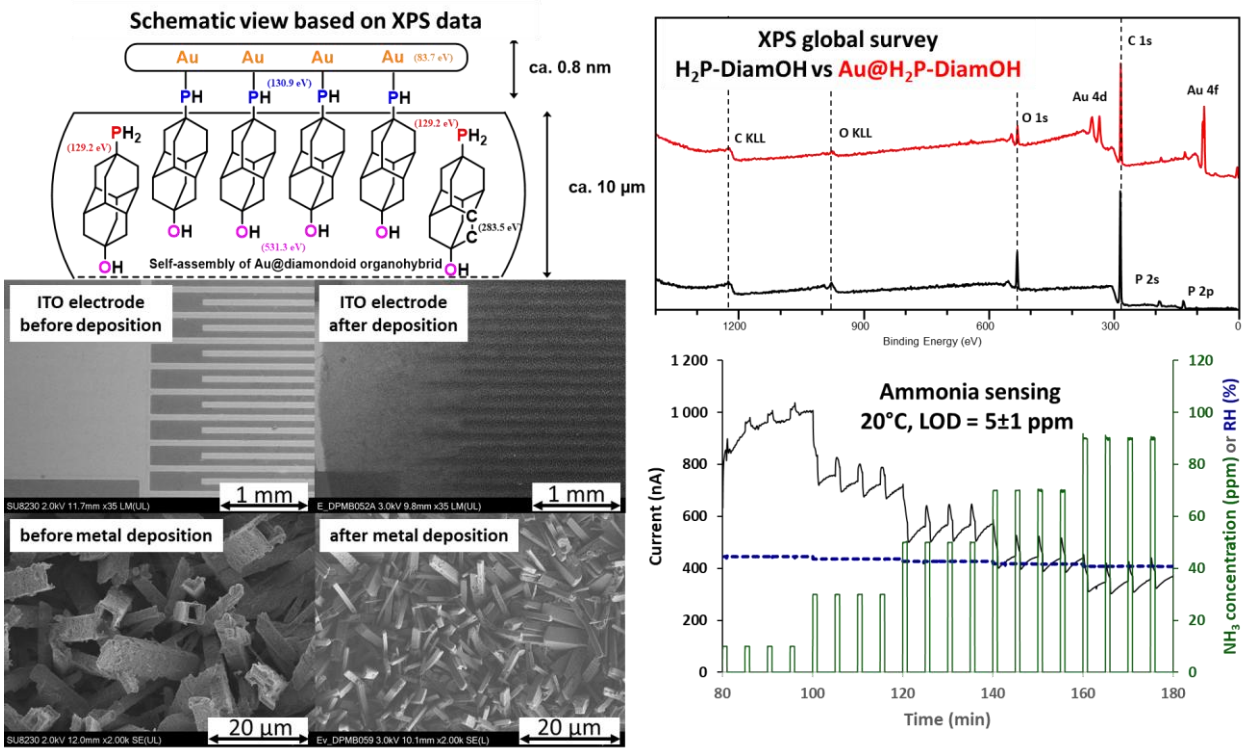

References and Notes

[1]. a) W. L. Noorduin, A. Grinthal, L. Mahadevan, J. Aizenberg, *Science* **2013**, *340*, 832; b) G. M. Whitesides, B. Grzybowski, *Science* **2002**, *295*, 2418.

[2]. a) G. Rogez, C. Massobrio, P. Rabu, M. Drillon, *Chem. Soc. Rev.* **2011**, *40*, 1031; b) R. Costi, A. E. Saunders, U. Banin, *Angew. Chem. Int. Ed.* **2010**, *49*, 4878; c) C. Zhu, S. Dong, *Nanoscale* **2013**, *5*, 10765; d) M. Faustini, L. Nicole, E. Ruiz-Hitzky, C. Sanchez *Adv. Funct. Mater.* **2018**, *28,* 1704158.

[3]. a) A. Bétard, R. A. Fischer, *Chem. Rev.* **2012**, *112*, 1055; b) O. Shekhah, H. Wang, S. Kowarik, F. Schreiber, M. Paulus, M. Tolan, C. Sternemann, F. Evers, D. Zacher, R. A. Fischer, C. Wöll, *J. Am. Chem. Soc.* **2007**, *129*, 15118; c) A. Umemura, S. Diring, S. Furukawa, H. Uehara, T. Tsuruoka, S. Kitagawa, *J. Am. Chem. Soc.* **2011**, *133*, 15506; d) J.-L. Zhuang, M. Kind, C. M. Grytz, F. Farr, M. Diefenbach, S. Tussupbayev, M. C. Holthausen, A. Terfort, *J. Am. Chem. Soc.* **2015**, *137*, 8237; e) H. O. Nasrallah, J.-C. Hierso, *Chem. Mater.* **2019**, *31*, 619.

[4]. a) X. Li, W. Cai, J. An, S. Kim, J. Nah, D. Yang, R. Piner, A. Velamakanni, I. Jung, E. Tutuc, S. K. Banerjee, L. Colombo, R. S. Ruoff, *Science* **2009**, *324*, 1312; b) Y. Kim, J. Lee, M. S. Yeom, J. W. Shin, H. Kim, Y. Cui, J. W. Kysar, J. Hone, Y. Jung, S. Jeon, S. M. Han, *Nat. Commun.* **2013**, *4*, 2114; c) C. Xu, X. Wang, J. Zhu, *J. Phys. Chem. C* **2008**, *112*, 19841; d) F.-X. Xiao, J. Miao, B. Liu, *J. Am. Chem. Soc.* **2014**, *136*, 1559; e) B. F. Machado, P. Serp, *Catal. Sci. Technol.* **2012**, 2, 54; f) V. Georgakilas, J. N. Tiwari, K. C. Kemp, J. A. Perman, A. B. Bourlinos, K. S. Kim, R. Zboril, *Chem. Rev.* **2016**, *116*, 5464.

[5]. a) J. Kong, M. G. Chapline, H. Dai, *Adv. Mater.* **2001**, 13, 1384; b) V. Subramanian, E. E. Wolf, P. V. Kamat, *J. Am. Chem. Soc.* **2004**, *126*, 4943; c) G. G. Wildgoose, C. E. Banks, R. G. Compton, *Small* **2006**, *2*, 182.

[6]. a) A. L. Balch, K. Winkler, *Chem. Rev.* **2016**, *116*, 3812; b) S. Bhattacharya, S. K. Samanta, *Chem. Rev.* **2016**, *116*, 11967.

[7]. a) Y. Liang, M. Ozawa, A. Krueger, *ACS Nano* **2009**, *3*, 2288; b) W. L. Yang, J. D. Fabbri, T. M. Willey, J. R. I. Lee, J. E. Dahl, R. M. K. Carlson, P. R. Schreiner, A. A. Fokin, B. A. Tkachenko, N. A. Fokina, W. Meevasana, N. Mannella, K. Tanaka, X. J. Zhou, T. van Buuren, M. A. Kelly, Z. Hussain, N. A. Melosh, Z.-X. Shen, *Science* **2007**, *316*, 1460; c) W. A. Clay, Z. Liu, W. Yang, J. D. Fabbri, J. E. Dahl, R. M. K. Carlson, Y. Sun, P. R. Schreiner, A. A. Fokin, B. A. Tkachenko, N. A. Fokina, P. A. Pianetta, N. Melosh, Z.-X. Shen, *Nano Lett.* **2009**, *9*, 57; d) K. T. Narasimha, C. Ge, J. D. Fabbri, W. Clay, B. A. Tkachenko, A. A. Fokin, P. R. Schreiner, J. E. Dahl, R. M. K. Carlson, Z. X. Shen, N. A. Melosh, *Nat. Nanotechnol.* **2016**, *11*, 267; e) F. H. Li, J. D. Fabbri, R. I. Yurchenko, A. N. Mileshkin, J. N. Hohman, H. Yan, H. Yuan, I. C. Tran, T. M. Willey, M. Bagge-Hansen, J. E. P. Dahl, R. M. K. Carlson, A. A. Fokin, P. R. Schreiner, Z.-X. Shen, N. A. Melosh, *Langmuir* **2013**, *29*, 9790; f) T. Petit, H. A. Girard, A. Trouve, I. Batonneau-Gener, P. Bergonzo, J.-C. Arnault, *Nanoscale* **2013**, 5, 8958; g) A. B. Lysenko, G. A. Senchyk, J. Lincke, D. Lassig, A. A. Fokin, E. D. Butova, P. R. Schreiner, H. Krautscheid, K. V. Domasevitch, *Dalton Trans.* **2010**, *39*, 4223; h) B. E. K. Barth, B. A. Tkachenko, J. P. Eußner, P. R. Schreiner, S. Dehnen, *Organometallics* **2014**, *33*, 1678.

[8]. M. A. Gunawan, O. Moncea, D. Poinsot, M. Keskes, B. Domenichini, O. Heintz, R. Chassagnon, F. Herbst, R. M. K. Carlson, J. E. P. Dahl, A. A. Fokin, P. R. Schreiner, J.-C. Hierso, *Adv. Funct. Mater.* **2018**, *28*, 1705786.

[9]. O. Moncea, J. Casanova-Chafer, D. Poinsot, L. Ochmann, C. D. Mboyi, H. O. Nasrallah; E. Llobet, I. Makni, M. El Atrous, S. Brandès, Y. Rousselin, B. Domenichini, N. Nuns, A. A. Fokin, P. R. Schreiner, J.-C. Hierso, *Angew. Chem., Int. Ed.* **2019**, *58*, 9933.

[10]. J. Zhang, X. Liu, S. Wu, H. Xu, B. Cao, *Sens. Actuators B Chem.* **2013**, *186*, 695.

[11]. Z. Li,J. Chen, L. Chen, M. Guo, Y. Wu, Y. Wei, J. Wang, X. Wang, *ACS Appl. Mater. Interfaces* **2020**, *12*, 55056.

[12]. S. Pandey, K. K. Nanda, *ACS Sens.* **2016**, *1*, 55.

[13]. G. Chen, Y. Yuan, M. Lang, Z. Lv, W. Ma, N. Gu, H. Liu, J. Fang, H. Zhang, Y. Cheng, *Appl. Surf. Sci.* **2022**, *598*, 153821.

[14]. C. Liu, H. Tai, P. Zhang, Z. Ye, Y. Su, Y. Jiang, *Sens. Actuators B Chem.* **2017**, *246*, 85.

[15]. S. Li, Y. Diao, Z. Yang, J. He, J. Wang, C. Liu, F. Liu, H. Lu, X. Yan, P. Sun, G. Lu, *Sens. Actuators B Chem.* **2018**, *276*, 526.

[16]. D. Zhang, Z. Yang, P. Li, M. Pang, Q. Xue, *Nano Energy* **2019**, *65*, 103974.

[17]. H. Yan, P. Song, S. Zhang, J. Zhang, Z. Yang, Q. Wang, *Ceram. Int.* **2016**, *42*, 9327.

[18]. L. Zhang, Z. Li, J. Yang, J. Zhou, Y. Zhang, H. Zhang, Y. Li, *ACS Sens.* **2022**, *7*, 1183.

[19]. B. Cho, A. R. Kim, D. J. Kim, H.-S. Chung, S. Y. Choi, J.-D. Kwon, S. W. Park, Y. Kim, B. H. Lee, K. H. Lee, D.-H. Kim, J. Nam, M. G. Hahm, *ACS Appl. Mater. Interfaces* **2016**, *8*, 19635.

[20]. K. Shingange, Z. P. Tshabalala, O. M. Ntwaeaborwa, D. E. Motaung, G. H. Mhlongo, *J. Colloid Interface Sci.* **2016**, *479*, 127.

[21]. Y. Tu, C. Kyle, H. Luo, D.-W. Zhang, A. Das, J. Briscoe, S. Dunn, M.-M. Titirici, S. Krause, *ACS Sens.* **2020**, *5*, 3568.

[22]. Q. A. Drmosh, *Chem. Phys. Lett.* **2022**, *790*, 139355.

[23]. D. Punetha, S. K. Pandey, *IEEE Trans. Electron Devices* **2019**, *66*, 3560.

[24]. M. Takács,D. Zámbó, A. Deák,A. E. Pap, I. Bársony, *Procedia Eng.* **2015**, *120*, 1128.

[25]. A. F. Ahmed, M. R. Abdulameer, M. M. Kadhim, F. A.-H. Mutlak, *Optik* **2022**, *249*, 168260.

[26]. C. N. Xu, N. Miura, Y. Ishida, K. Matsuda, N. Yamazoe, *Sens. Actuators B Chem.* **2000**, *65*, 163.

[27]. C. Wang, B. Yang, R. Xiao, H. Liu, H. Yu, J. Wang, F. Xia, J. Xiao, *J. Electrochem. Soc.* **2020**, *167*, 027540.

[28]. L. Wang, W. Meng, Z. He, W. Meng, Y. Li, L. Dai, *Sens. Actuators B Chem.* **2018**, *272*, 219.

[29]. T. Sato, H. Ikeda, N. Miura, *ECS Electrochem. Lett.* **2014**, *3*, B13.

[30]. B. Wang, S. Yao, F. Liu, Y. Guan, X. Hao, X. Liang, F. Liu, P. Sun, Y. Wang, H. Song, G. Lu, *Sens. Actuators B Chem.* **2017**, *243*, 1083.

[31]. B. Yang, C. Wang, R. Xiao, H. Yu, J. Wang, H. Liu, F. Xia, J. Xiao, *Mater. Chem. Phys.* **2020**, *239*, 122302.

[32]. A. Tricoli, M. Righettoni, A. Teleki, *Angew. Chem. Int. Ed.* **2010**, *49*, 7632.

[33]. M. A. Gunawan, D. Poinsot, B. Domenichini, C. Dirand, S. Chevalier, A. A. Fokin, P. R. Schreiner, J.-C. Hierso, *Nanoscale* **2015**, *7*, 1956.

[34]. a) H. Schmidbaur, A. Shiotani, *Chem. Ber.*, **1971**, *104*, 2821; b) J. R. Heath, P.F. Seidler, *Mat. Res. Soc. Symp. Proc.*, **1993**, *282*, 359; c) J. Messelhäuser E. B. Flint, H. Suhr, *Applied Surf. Sci.*, **1992**, *54*, 64.

[35]. See for instance: S.-J. Cho, J.-C. Idrobo, J. Olamit, K. Liu, N. D. Browning, S. M. Kauzlarich, *Chem. Mater.* **2005**, *17*, 3181, and references therein.

[36]. M. P. Seah, G. C. Smith, M. T. Anthony, *Surf. Interface Anal.*, **1990**, *15*, 293.

[37]. a) R. Ye, A. V. Zhukhovitskiy, R. V. Kazantsev, S. C. Fakra, B. B. Wickemeyer, F. D. Toste, G. A. Somorjai, *J. Am. Chem. Soc*., **2018**, *140*, 4144; b) M. Kanehara, E. Kodzuka, T. Teranishi, *J. Am. Chem. Soc.* **2006**, *128*, 13084; c) N. Kruse, S. Chenakin, *Appl. Catal., A* **2011**, *391*, 367.

[38]. M. Quintiliani, M. Bassetti, C. Pasquini, C. Battocchio, M. Rossi, F. Mura, R. Matassa, L. Fontana, M. V. Russo, I. Fratoddi, *J. Mater. Chem. C* **2014**, *2*, 2517.

[39]. H. O. Nasrallah, Y. Min, E. Lerayer, T.-A. Nguyen, D. Poinsot, J. Roger, S. Brandès, O. Heintz, P. Roblin, F. Jolibois, R. Poteau, Y. Coppel, M. L. Kahn, I. C. Gerber, M. R. Axet, P. Serp, J.-C. Hierso, *JACS Au,* **2021**, *1*, 187.

[40]. H. Kitagawa, N. Kojima, T. Nakajima, *J. Chem. Soc., Dalton Trans* **1991**, 3121.

[41]. J.-J. Pireaux, M. Liehr, P. Thiry, J.-P. Delrue, R. Caudano, *Surf. Sci.*, **1984**, *141*, 22

[42]. T. Li, G. Fu, J. Su, Y. Wang,Y. Lv, X. Zou, X. Zhu, L. Xu, D. Sun, Y. Tang, *Electrochim. Acta*, **2017**, *231*, 13.

[43]. The photoemission signals C1s and Auger C KLL correspond to very different kinetic energies of *ca.* 1200 eV and 240 eV, respectively. Their attenuation through the gold film is different and can be expressed as $I = I_0 e^{-d/\lambda}$, where I is the intensity of the detected signal, I_0 is the intensity of the signal emitted by the diamondoid deposit when it is not covered by gold and λ is the inelastic mean free path (IMFP) of the electrons emitted through gold. For each energy, *i. e.* for each signal, λ can be easily determined using the TPP-2M model (Tanuma-Powell-Penn, see *Surf. Interface Anal*. **1997**, *25*, 25). Intensity ratio rather than direct intensities are used. The intensities of the signals detected for the core level C1s and for the Auger signal C KLL are written, respectively: $I^{C1s} = I_0^{C1s} e^{-d/\lambda^{C1s}}$ and $I^{CKLL} = I_0^{CKLL} e^{-d/\lambda^{CKLL}}$

(I^{C1s} and I^{CKLL} are the intensity of the detected signals C1s and CKLL, respectively), I_0^{C1s} and I_0^{CKLL} are the intensity of the signals C1s and CKLL from the native diamondoid deposit and λ^{C1s} and λ^{CKLL} are the inelastic mean free path (IMFP) of the electrons, which constitute the signals C1s and CKLL through gold film. The ratio are expressed as $\frac{I^{C1s}}{I^{CKLL}} = \frac{I_0^{C1s}}{I_0^{CKLL}} \times \frac{e^{-d/\lambda^{C1s}}}{e^{-d/\lambda^{CKLL}}}$

and $\frac{I^{C1s}}{I^{CKLL}} = \frac{I_0^{C1s}}{I_0^{CKLL}} \times e^{(\lambda^{CKLL} - \lambda^{C1s})/d}$ from which the thickness d can be extracted. The determination of the ratio of the intensities of the signals C1s and CKLL is measured for a given coated sample and the same intensity ratio for a sample without gold deposit. Extraction of the

thickness d can be achieved from O1s and OKLL signals following the same principle. The difference in energy between the O1s and OKLL signals being less important than between C1s and CKLL, the result obtained may be less precise.

[44]. See for instance : M. B. E. Griffiths, P. J. Pallister, D. J. Mandia, S. T. Barry, *Chem. Mater.* **2016**, *28*, 44 and references therein.

[45]. From a mechanistic viewpoint, charges need to flow across the resistive material, as depicted in Figure 7, for joinning the gold layer. Electrons, provided by an incorporated DC voltage supply and connected to one of interdigitated electrode, pass through the 10 µm thickness of the sensitive material (diamondoid scaffolding) in order to achieve the less resistive gold monolayer and finish its path at the second interdigitated electrode by recrossing the resistive and sensitive material. This energy shortcut prevents the electrons from traveling a lateral interelectrode distance of *ca.* 75 µm in a mainly resistive diamondoid material, and nicley explains the enhancement of the measured electric current using the gold composite.

[46]. Z. Şahin, R. Meunier-Prest, F. Dumoulin, A. Kumar, Ü. Isci, M. Bouvet, *Sens. Actuators B Chem.*, **2021**, *332*, 129505.

[47]. A. Kumar, R. Meunier-Prest, F. Herbst, O. Heintz, E. Lesniewska, M. Bouvet, *Chem. Eng. J.*, **2022**, *436*, 135207.

[48]. P. Gaudillat, A. Wannebroucq, J.-M. Suisse, M. Bouvet, *Sens. Actuators B Chem.*, **2016**, *222*, 910.